

# Understanding the Formation of $\text{CaAl}_2\text{Si}_2\text{O}_8$ in Melilite-Based Glass-Ceramics: Combined Diffraction and Spectroscopic Studies

Amarnath R. Allu,<sup>\*,†,‡,§</sup> Sathravada Balaji,<sup>†</sup> Dilshat U. Tulyaganov,<sup>‡,§</sup> Glenn C. Mather,<sup>||</sup> Fabian Margit,<sup>⊥</sup> María J. Pascual,<sup>||</sup> Renée Siegel,<sup>#</sup> Wolfgang Milius,<sup>¶</sup> Jürgen Senker,<sup>#</sup> Dmitrii A. Agarkov,<sup>∇</sup> Vladislav V. Kharton,<sup>∇</sup> and José M. F. Ferreira<sup>\*,†,‡,§</sup>

<sup>†</sup>Glass Science and Technology Section, CSIR—Central Glass and Ceramic Research Institute, 700032 Kolkata, India

<sup>‡</sup>Department of Materials and Ceramics Engineering, CICECO, University of Aveiro, 3810-193 Aveiro, Portugal

<sup>§</sup>Turin Polytechnic University in Tashkent, 17, Small Ring, 100095 Tashkent, Uzbekistan

<sup>||</sup>Instituto de Cerámica y Vidrio (CSIC), C/Kelsen 5, Campus de Cantoblanco, 28049 Madrid, Spain

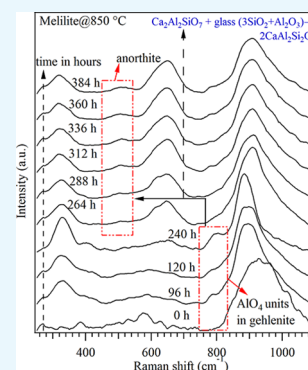
<sup>⊥</sup>Centre for Energy Research, Konkoly-Thege Street 29-33, 1121 Budapest, Hungary

<sup>#</sup>Inorganic Chemistry III and <sup>¶</sup>Inorganic Chemistry I, University of Bayreuth, 95440 Bayreuth, Germany

<sup>∇</sup>Institute of Solid State Physics RAS, 142432 Chernogolovka, Moscow District, Russia

## Supporting Information

**ABSTRACT:** An assessment is undertaken for the formation of anorthite crystalline phase in a melilite-based glass composition (CMAS:  $38.7\text{CaO}-9.7\text{MgO}-12.9\text{Al}_2\text{O}_3-38.7\text{SiO}_2$  mol %), used as a sealing material in solid oxide fuel cells, in view of the detrimental effect of anorthite on the sealing properties. Several advanced characterization techniques are employed to assess the material after prolonged heat treatment, including neutron powder diffraction (ND), X-ray powder diffraction (XRD),  $^{29}\text{Si}$  and  $^{27}\text{Al}$  magic-angle spinning nuclear magnetic resonance (MAS-NMR), and in situ Raman spectroscopy. ND,  $^{29}\text{Si}$  MAS-NMR, and  $^{27}\text{Al}$  MAS-NMR results revealed that both Si and Al adopt tetrahedral coordination and participate in the formation of the network structure. In situ XRD measurements for the CMAS glass demonstrate the thermal stability of the glass structure up to  $850\text{ }^\circ\text{C}$ . Further heat treatment up to  $900\text{ }^\circ\text{C}$  initiates the precipitation of melilite, a solid solution of akermanite/gehlenite crystalline phase. Qualitative XRD data for glass-ceramics (GCs) produced after heat treatment at  $850\text{ }^\circ\text{C}$  for 500 h revealed the presence of anorthite along with the melilite crystalline phase. Rietveld refinement of XRD data indicated a high fraction of glassy phase ( $\sim 67\%$ ) after the formation of crystalline phases. The  $^{29}\text{Si}$  MAS-NMR spectra for the CMAS-GC suggest the presence of structural units in the remaining glassy phase with a polymerization degree higher than dimer units, whereas the  $^{27}\text{Al}$  MAS-NMR spectra revealed that most  $\text{Al}^{3+}$  cations exhibit a 4-fold coordination. In situ Raman spectroscopy data indicate that the formation of anorthite crystalline phase initiated after 240 h of heat treatment at  $850\text{ }^\circ\text{C}$  owing to the interaction between the gehlenite crystals and the remaining glassy phase.



## 1. INTRODUCTION

In recent years, planar-solid oxide fuel cells (p-SOFC) have been considered as one of the most efficient and versatile power generation systems. However, a major hurdle that needs to be overcome for their commercialization is the development of a hermetic high-temperature sealing material.<sup>1–4</sup> Durable sealants are required to prevent gas mixing between the anode and cathode compartments, to bond the cell stacks, and to provide electrical insulation. Among the various types of sealing materials, glasses and glass-ceramics (GCs) are considered to be the most efficient and attractive sealants for SOFCs because of their ability to form hermetic and durable seals at high temperatures and at relatively low cost.<sup>3–6</sup>

Glass-based materials are promising for many technological applications because of their flexible chemical compositions combined with ease of handling and manufacturing and relative cheapness.<sup>4,7</sup> Glasses are known to be more stable at room

temperature (RT) because of the short-range order of the bonding ions.<sup>8</sup> Although the stability of vitreous phase usually decreases with increasing temperature or during isothermal heat treatments,<sup>3</sup> the thermal, mechanical, and electrical properties of the heat-treated materials may be improved through the formation of crystalline phases, forming GCs. The chemical formulae of the formed crystalline phases are closely related to that of the parent glass composition. In general, GCs are polycrystalline materials, normally obtained from parent glasses by partial devitrification.<sup>9</sup> However, the polymorphism of the crystalline phase is another important feature that can affect the properties of GCs. For example, barium-rich, aluminosilicate-based glasses are known to exhibit appropriate

Received: May 12, 2017

Accepted: July 26, 2017

Published: September 28, 2017

coefficients of thermal expansion (CTEs) for their operation as sealing materials in SOFCs.<sup>10</sup> However, these glasses have a tendency to devitrify at around 800–850 °C, resulting in the appearance of hexacelsian ( $\text{BaAl}_2\text{Si}_2\text{O}_8$ ). During SOFC operation, the crystalline phase gradually transforms into its monoclinic polymorph, which has a low CTE<sup>11</sup> associated with the deterioration of the mechanical properties. Hence, understanding the formation and development of crystalline phases in GC-based materials during devitrification is of crucial importance for industrial applications.

In search of a suitable glass sealant material for p-SOFCs, with high chemical resistance and appropriate CTE, we have investigated a glass composition in the  $\text{CaO-MgO-Al}_2\text{O}_3\text{-SiO}_2$  (CMAS) system and within the primary crystallization field of akermanite ( $\text{Ca}_2\text{MgSi}_2\text{O}_7$ )/gehlenite ( $\text{Ca}_2\text{Al}_2\text{SiO}_7$ ).<sup>12</sup> Nevertheless, the formation of triclinic anorthite ( $\text{CaAl}_2\text{Si}_2\text{O}_8$ ), an important member of the feldspar family, as the second dominant crystalline phase after 300 h of heat treatment at 850 °C, puts into question the reliability of CMAS as a glass seal. The most important aspects of anorthite in relation to sealant applications are the temperature-induced reversible phase transformation and its CTE value. Anorthite adopts triclinic symmetry (space group  $P\bar{1}$ ) at RT but transforms to the body-centered  $\bar{I}$  space group at a transition temperature ( $T_c$ ) of approximately 240 °C.<sup>13–15</sup> The framework structure is more crumpled in the  $P\bar{1}$  symmetry and more expanded in the  $\bar{I}$  phase.<sup>16</sup> Moreover, the apparent CTE value of anorthite was reported to be  $11 \times 10^{-6} \text{ K}^{-1}$  within the temperature range 20–1000 °C.<sup>17</sup> This contrasts with the value of  $\sim 5.3 \times 10^{-6} \text{ K}^{-1}$  determined within the temperature range of 250–800 °C from high-resolution data of the  $\bar{I}$  phase.<sup>18–20</sup> Hence, the CMAS glass may not be completely satisfactory in real SOFC operating conditions under repeated thermal cycling, under which even a minor mismatch in the CTE gives rise to thermal stresses in the GC sealant during startup and shutdown.<sup>5,6</sup> Although the induced stresses may not cause an immediate seal failure, they may generate cracks during long-term operation. The formation of undesired crystalline phases in the technologically applicable GC materials therefore should be avoided.

In view of the above, we endeavor to better understand the formation of undesired secondary crystalline phase in CMAS-GC-based sealant materials. In the present study, a range of structurally sensitive investigation tools are employed to this end, including neutron powder diffraction (ND), X-ray powder diffraction (XRD), <sup>29</sup>Si and <sup>27</sup>Al magic-angle spinning nuclear magnetic resonance (MAS-NMR), and in situ Raman spectroscopy.

## 2. RESULTS

**2.1. Glass Structure.** Figure 1 shows the total experimental structure factor  $S(Q)$  (dotted line) and simulated  $S(Q)$  from the reverse Monte Carlo (RMC) model (continuous line) for the CMAS glass composition derived from neutron diffraction for  $Q$  values in the range 0.95–9.5 Å<sup>-1</sup>. It is known that the ND technique is highly sensitive to hydrogen, the presence of which in glass samples due to hydrolysis results in well-identified peaks in the final ND spectrum. Here, the ND pattern reveals that the specimens are fully amorphous, and no hydrogen was detected. The most striking feature of the  $S(Q)$  data is the relatively high intensity and sharp distribution of the first and second peaks of the CMAS glass, which is a fingerprint of a network structure formed by well-defined units. The intensity

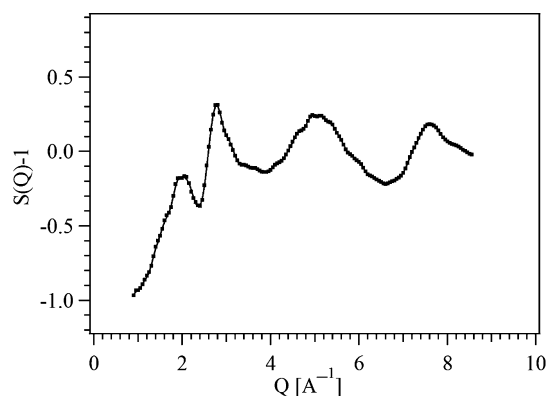


**Figure 1.** Neutron diffraction structure factors of CMAS glass: experimental data (dots) and RMC simulation (solid black line).

of the third and fourth peaks of the glass becomes broader, indicating a complex network structure.

Several partial atomic pair correlation functions and coordination number distributions have been revealed with moderately good stability. Herein, we focus on the characteristic features of oxygen coordination of the Si and Al network formers by analyzing the polyhedral units and their linkages. The derived atomic pair correlation functions  $g_{ij}(r)$  and the coordination number distributions from the RMC simulations for the CMAS glass composition are shown in Figures 2 and 3, respectively. In general, the position and width of the peak in the pair correlation function  $g_{ij}(r)$  reflect the value and the distribution of the distances for different atomic correlations, respectively. The oxygen-linked  $g_{i-O}(r)$  (where  $i = \text{Ca, Mg, Al, Si, and O}$ ) are shown in the plots of Figure 2. The peaks for Si–O, Al–O, Mg–O, and Ca–O pairs are located at 1.6, 1.75, 1.7, and 2.35 Å, respectively. These values concur with the characteristic lengths of 1.6 Å for Si–O and 1.75 Å for Al–O for multicomponent aluminosilicate glasses.<sup>21</sup>

The peak corresponding to Si–O correlations is narrow, whereas those corresponding to Al–O, Mg–O, and Ca–O are broader and more asymmetric, resulting from a larger distribution of distances between oxygen and aluminum, magnesium, and calcium. From the coordination number distribution of Si and Al, shown in Figure 3, it is clear that the CMAS glass contains a high fraction of 4-fold-coordinated Si and Al atoms, which is consistent with a silicate network formed from corner-sharing  $\text{SiO}_4$  tetrahedra. For the CMAS sample, an average coordination number  $\text{CN}_{\text{Si-O}} = 3.83 \pm 0.2$  (Figure 3) is obtained. Considering the  $g_{\text{Si-O}}(r)$  distribution (Figure 2d), it is reasonable to consider that the shorter distance of 1.6 Å can be attributed to the  $\text{SiO}_4$  units which form the network or partake in the network formation. The initial RMC constraint of Si connectivity is, therefore, justified because the Si atoms are coordinated on average to four oxygen neighbors.

**2.2. In Situ XRD Studies.** Figure 4 shows the high-temperature (HT)-XRD patterns of the CMAS glass recorded from RT to 900 °C. The CMAS glass is highly stable and amorphous up to 850 °C. However, from 850 to 900 °C, low-intensity XRD reflections are observed, indicating that the crystals have started to precipitate. The observed XRD reflections correspond to the melilite-based akermanite/gehlenite crystals (ICDD: 76-7527). Notably, a slow cooling rate ( $\approx 2 \text{ K min}^{-1}$ ) from 900 °C to RT led to an increase in the intensity of the XRD reflections. However, no additional XRD

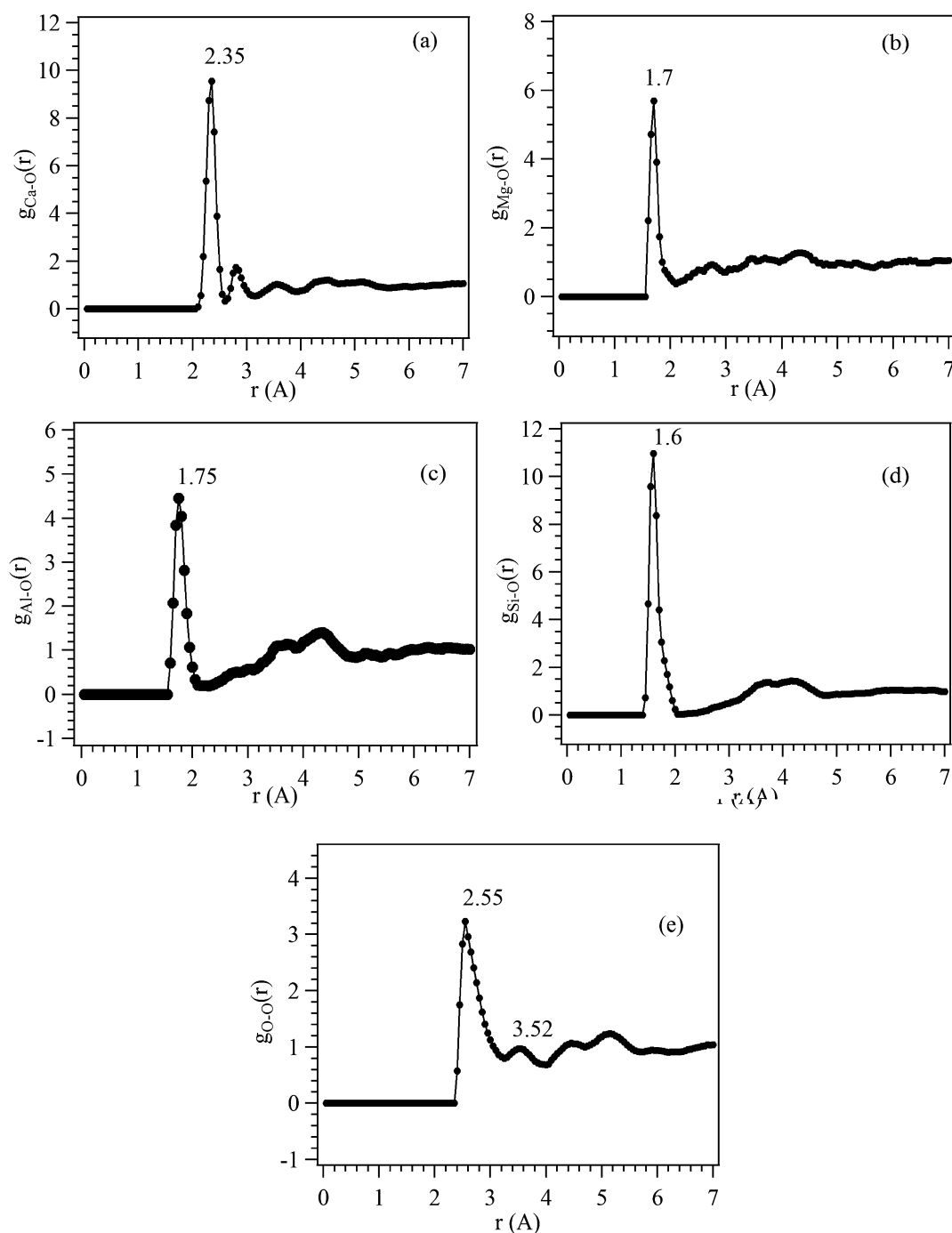


**Figure 2.** Oxygen-linked partial atomic pair correlation functions obtained from the RMC modeling for the CMAS glass: (a) Ca–O, (b) Mg–O, (c) Al–O, (d) Si–O, and (e) O–O.

reflections corresponding to new crystalline phases were observed during the cooling process. The position of the HT-XRD reflections is similar to that of the XRD reflections obtained for the glass-powder compacts sintered at 900 °C for 1 h, although differences in intensities are observed. The time for the growth of anorthite nuclei from their own melts at 900 and 1050 °C has been reported as 92 and 48 h, respectively.<sup>22</sup> On the basis of previous studies<sup>12,23,24</sup> and from the in situ XRD results, it is confirmed that a thermal treatment of 900 °C for 1 h is sufficient to grow the melilite-based nucleus from the CMAS glass composition.

**2.3. Quantitative Rietveld Refinement.** Quantitative phase analysis proceeded with the Rietveld refinement of melilite-based phase, employing a composition of  $\text{Ca}_2\text{Mg}_{0.35}\text{Al}_{1.3}\text{Si}_{1.35}\text{O}_7$  and anorthite,  $\text{CaAl}_2\text{Si}_2\text{O}_8$ , in the space groups  $P4_2/m$  and  $P\bar{1}$ , respectively. The structural models were based on published structural data.<sup>25</sup> Because of the large number of refinable parameters in the two structures, thermal vibration factors, occupancies, and certain atomic positions were fixed throughout the refinement. The observed diffraction pattern and difference between the observed and calculated data on the termination of refinement are shown in Figure 5. Selected structural parameters and agreement factors are given

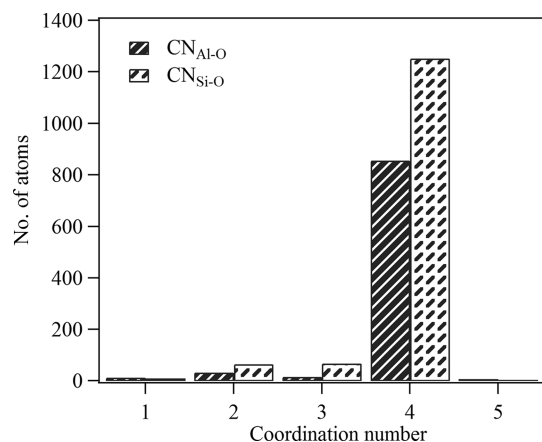


**Figure 3.** Coordination number distributions,  $CN_{ij}$ , as obtained from the RMC modeling for the CMAS glass.

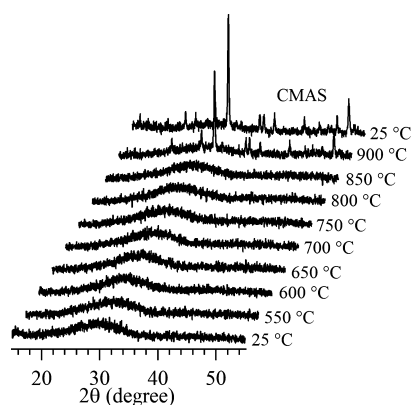


**Figure 4.** XRD diffractograms of the CMAS glass-powder compacts obtained during the heat treatment from RT to 900 °C.

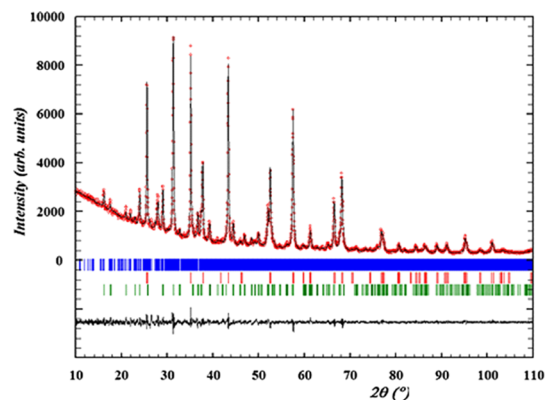


**Figure 5.** Observed XRD profiles and difference between the observed and calculated data of the CMAS-GC obtained on heat treatment at 850 °C for 500 h with  $Al_2O_3$  as the internal standard. The vertical bars represent the Bragg peaks of anorthite (blue), alumina (red), and melilite (green).

in Table 1. The calculated amounts of melilite and anorthite were 25.6 and 8.1 wt %, respectively, with the remaining 66.3 wt % amorphous phase.

**2.4.  $^{29}Si$  and  $^{27}Al$  MAS-NMR Spectroscopic Studies.**  $^{29}Si$  and  $^{27}Al$  MAS-NMR spectra of glass and GC samples are displayed in Figure 6. The  $^{29}Si$  MAS-NMR spectrum of the CMAS glass shows a single broad resonance Q-site distribution with the center of gravity (CG) at  $-78$  ppm. Numerous studies

**Table 1.** Selected Structural Parameters and Agreement Factors for CMAS-GC Obtained from XRD Data<sup>a</sup>

	CMAS-GC	
	anorthite, $P\bar{1}$	melilite, $P\bar{4}2_1m$
$a$ (Å)	8.243(3)	7.7421(4)
$b$ (Å)	12.863(6)	
$c$ (Å)	14.154(6)	5.0416(5)
$\alpha$	91.01(5)	
$\beta$	115.08(4)	
$\gamma$	88.15(4)	
$V$ (Å <sup>3</sup> )	1359(1)	302.20(4)

<sup>a</sup> $\chi^2 = 2.30$ ,  $R_p = 3.59\%$ ,  $R_{wp} = 4.70\%$ ,  $R_B$  (anorthite) = 10.2, and  $R_B$  (melilite) = 2.60.

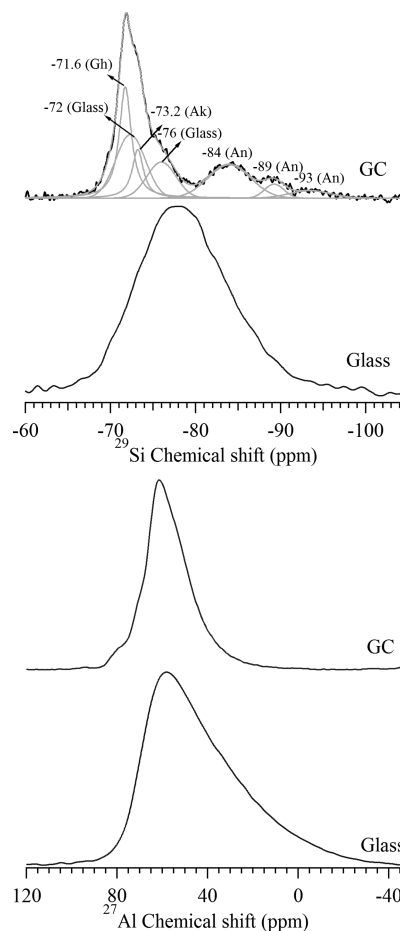


**Figure 6.**  $^{29}Si$  and  $^{27}Al$  MAS-NMR spectra of glass and GCs. Gh = gehlenite, Ak = akermanite, and An = anorthite.

indicate that  $SiO_4$  tetrahedra in glasses normally occur in more than one polymerization state, the distribution of which is a function of composition.<sup>26–28</sup> The appearance of CG at  $-78$  ppm indicates that this glass is mostly enriched in  $Q^1 + Q^2$  units, whereas other Q units including  $Q^n(mAl)$  units, where  $n$  (ranging from 0 to 4) is the number of bridging oxygens (BOs) associated with Si and  $m$  (ranging from 0 to 4) is the number of Al in the next-nearest neighbor (NNN), are below the detectable levels.<sup>29</sup> However,  $^{27}Al$  MAS-NMR can provide valuable information on the glass composition as the  $^{27}Al$  chemical shift is strongly dependent on the aluminum coordination.<sup>30</sup> The  $^{27}Al$  MAS-NMR spectrum of the CMAS glass exhibits a broad asymmetric peak with a tail toward

negative parts per million, which is a typical profile in disordered materials such as glass. The appearance of the peak at an isotropic shift of about 70 ppm (the isotropic shift is usually set on the left end of the spectra because of the second-order quadrupolar shift) but with a maximum at 59 ppm indicates that most of the Al resides in tetrahedral environments, consistent with the results obtained from the RMC simulation.<sup>31</sup> This is also confirmed by the satellite-transition magic-angle spinning (STMAS) spectra (Figure S1), in which only  $\text{AlO}_4$  sites are observed and no penta- or octahedrally coordinated Al environments are distinguishable.

Solid-state  $^{29}\text{Si}$  NMR spectra are highly sensitive to the number and type of silicon environments present within the crystal material, providing a direct correlation between the number of resonances and the number of crystallographically distinct silicon sites. For crystalline silicates, the  $^{29}\text{Si}$  chemical shift becomes more negative as the degree of polymerization increases.<sup>32,33</sup> However, the substitution of Al for Si on the tetrahedral sites of framework and sheet silicates caused the  $^{29}\text{Si}$  chemical shift to become less negative by 3–5 ppm per NNN Al.<sup>32–34</sup> Moreover, a careful comparison of NMR and diffraction results revealed that a change in the Si–O bond length of 0.001 Å produced a difference in the shift of ca. 1 ppm and a change of 1° in the Si–O–T bond angle led to changes in the  $^{29}\text{Si}$  solid-state chemical shift between ca. 0.3 and 0.9 ppm.<sup>35,36</sup>

Considerable differences are observed in the  $^{29}\text{Si}$  MAS-NMR spectra of the GC samples compared to those of the CMAS glass, most notably the presence in the former of two main components (Figure 6). The largest contribution found at  $\sim -71.9$  ppm corresponds to that of aluminum-rich melilite minerals, also observed in the XRD patterns,<sup>29,37</sup> whereas the smaller component located at  $-84$  ppm is typical of anorthite.<sup>38,39</sup> The presence of several overlapping peaks in the  $-71$  to  $-85$  ppm region can be easily explained by the presence of various types of silicate tetrahedral units surrounded by different cations in the melilite-type crystalline phase. However, deconvolution analysis reveals the appearance of four overlapping Gaussian peaks, which appear at  $-71.6$ ,  $-72$ ,  $-73.2$ , and  $-76$  ppm, in the  $-71$  to  $-85$  ppm range. In addition to the peak at  $-84$  ppm, the smaller component of the CMAS-GC sample exhibits two shoulders at  $-89$  and  $-93$  ppm. It is worth mentioning that the smaller component of the GC sample is similar to but comparatively less well-resolved than that of the synthetic anorthite synthesized from the parent glass after a heat treatment at  $1400$  °C for 179 h.<sup>39</sup>

Heat treatment at  $850$  °C for 500 h significantly reduced the width of the  $^{27}\text{Al}$  MAS-NMR spectrum of the glass (Figure 6), but the peak maximum remains at 56 ppm, indicating that Al is essentially unchanged with increasing time of thermal treatment. The similarity between the glass and the GC samples is not surprising because anorthite and melilite are the dominant crystalline phases in the GC, with most Al residing in tetrahedral sites with four BOs and four Si neighbors. By contrast, a small shoulder at 80 ppm appears in the GC sample, which is not evident in the glass. The  $^{27}\text{Al}$  peak maxima for  $^{\text{IV}}\text{Al}$  are known to fall in the range 75–80 ppm for aluminates.<sup>40</sup> The formation of linkages between two different tetrahedral aluminum sites existing in anorthite and in magnesium-rich melilite is another possible reason for the appearance of the shoulder at 80 ppm. This feature may correspond to the structural characteristic frequency of layer-lattice aluminosilicates, the structures of which consist of two-dimensional

octahedral  $\text{AlO}_6$  sheets alternating with tetrahedral  $\text{SiO}_4$  sheets, in which some replacement of Si by Al can also occur; the charge imbalance is compensated by the presence of interlayer cations.<sup>41</sup>

**2.5. Raman Studies.** Raman spectroscopy is widely used to investigate the structural changes in aluminosilicate glasses because of its capacity to distinguish crystalline phases and provide indirect information about the structural role of  $\text{Al}^{3+}$  ions.<sup>42</sup> Raman intensities from the vibrations of electrostatic bonds, generally appearing between modifier (M) cations and nonbridging oxygens (NBOs), are approximately 2 orders of magnitude less than those generated from the vibrations of covalent bonds between the network-former cations and BOs.<sup>42</sup> Because of this, the intermolecular vibration modes of silicate cations dominate the Raman spectra of silicate crystals and glasses. However, as explained in a previous report,<sup>26</sup> the bonding forces between the modifier cation and NBOs strongly influence the intensity of covalent bonds because greater covalent character between NBOs and the metal ion tends to reduce the degree of electron sharing in the Si–O<sup>−</sup> bonds. Such a behavior explains the variation in the intensity and the interaction between modifier cations and network formers with increasing heat treatment time.

The Raman spectrum of CMAS-GC heat-treated at  $850$  °C for 500 h, together with the spectra of akermanite and anorthite, is shown in Figure 7. Within the limits of

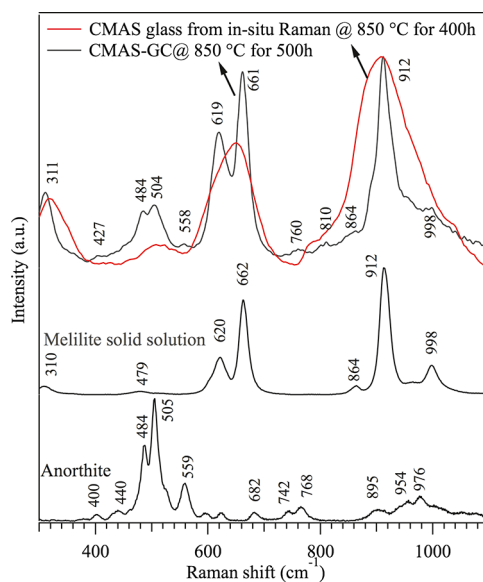


**Figure 7.** Comparison of Raman spectra of CMAS-GC heat-treated at  $850$  °C for 500 h with those of anorthite and melilite.

experimental error,  $\pm 2$   $\text{cm}^{-1}$ , the Raman frequencies observed from the CMAS-GC spectrum correspond well to the characteristic frequencies of both melilite-based akermanite/gehlenite<sup>43</sup> and anorthite crystalline phases.<sup>42</sup> The phase analysis is also consistent with the corresponding XRD results. The following features are identified as the corresponding frequencies of akermanite- and gehlenite-based crystalline phases: (i) the broad band with a peak position at  $912$   $\text{cm}^{-1}$  is attributed to a symmetric stretching motion of terminal NBOs of  $\text{SiO}_4$ , which can be represented as  $\nu_s(\text{SiO}_3^-)$ ; (ii) the band at  $988$   $\text{cm}^{-1}$  is attributed to an asymmetric stretching vibration of BOs situated between two tetrahedra (T), which can be represented as  $\nu_{\text{as}}(\text{SiOSi})$ ; (iii) the bands at 661 and 619

$\text{cm}^{-1}$  are ascribed to the symmetric stretching vibrations of BOs  $\nu_s(\text{TOT})$ , where T = Si or Al, present in akermanite and gehlenite crystalline phases, respectively;<sup>43</sup> and (iv) the vibration band in the lower frequency region at  $311 \text{ cm}^{-1}$  is attributed to a lattice vibrational mode. The broad band with peak positions at  $484$  and  $504 \text{ cm}^{-1}$  corresponds to the symmetric stretching vibrations of BOs  $\nu_s(\text{TOT})$ , where T = Si or Al, in the anorthite crystalline phase.<sup>42</sup> The peak appearing at  $790 \text{ cm}^{-1}$  is attributed to a vibration of Al in the tetrahedral form.<sup>42,43</sup>

Figure 8 shows the Raman spectra of CMAS glass powders in the region  $300\text{--}1100 \text{ cm}^{-1}$  recorded on varying the heat

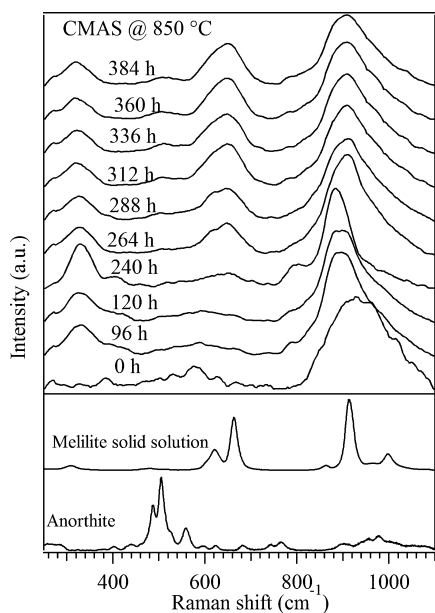


**Figure 8.** In situ Raman spectra for GC heat-treated at  $850 \text{ }^\circ\text{C}$  for 400 h.

treatment time from 0 to 400 h at  $850 \text{ }^\circ\text{C}$ . The spectrum at 0 h shows a broad resonance band, consistent with the amorphous nature of the glass. Thereafter, well-resolved peaks associated with the crystalline phase are observed with increasing heat treatment time. However, the peaks are not as well-resolved (the spectrum shown in red) as those observed for the CMAS-GC powder compact sample heat-treated at  $850 \text{ }^\circ\text{C}$  for 500 h (Figure 7). This suggests that powder compaction (decreasing porosity) favors crystallization as the number of crystals is expected to increase. It is worth mentioning that the peak positions are identical throughout the measured spectrum range in both the GCs.

The spectrum of the glass powder before heat treatment (0 h) exhibits an intense, asymmetric, broad peak at  $930 \text{ cm}^{-1}$  (Figure 8), which is attributed to the symmetric stretching of terminal NBOs  $\nu_s(\text{SiO}_3^-)$ . Whereas the intensity of this band decreases with increasing heat treatment time from 0 to 400 h, the broad area decreases from 0 to 240 h and then increases with further increasing heat treatment time up to 400 h. Correspondingly, the peak position shifts toward a lower wave number with increasing time of treatment from 0 to 240 h then shifts toward a higher wave number with increasing heat treatment time from 240 to 264 h, before stabilizing with further increasing time of treatment. A shoulder appearing at the low-frequency side of the  $\nu_s(\text{SiO}_3^-)$  band at  $\sim 790 \text{ cm}^{-1}$  is attributed to the  $\text{AlO}_4$  units present at a site with point group

symmetry  $\bar{4}$  in melilite. The intensity of this shoulder decreases with increasing time of heat treatment up to its disappearance after 240 h. Nevertheless, an additional new peak with very low intensity appears again at  $\sim 790 \text{ cm}^{-1}$  after 260 h, the intensity of which increases with increasing time of heat treatment. The second, high-intensity, broad band appearing at  $577 \text{ cm}^{-1}$  after 240 h of heat treatment is attributed to the symmetric stretching vibrations of BO situated between two Si tetrahedra, represented as  $\nu_s(\text{SiOSi})$ . A shoulder at  $647 \text{ cm}^{-1}$  accompanied by a band peaking at  $620 \text{ cm}^{-1}$  due to the symmetric stretching mode of  $\nu_s(\text{TOT})$  (where T = Si or Al) is also observed up to 288 h; these bands then tend to overlap with the  $\nu_s(\text{SiOSi})$  broad band with further increasing heat treatment time. The third intense band observed at  $311 \text{ cm}^{-1}$  corresponds to the lattice vibrational mode, which is not much influenced by increasing heat treatment time. All three strong bands, appearing at 912, 661, and  $311 \text{ cm}^{-1}$ , are characteristic frequencies of melilite, as reported previously.<sup>43</sup> In addition, bands of low intensity with the characteristic frequencies of anorthite<sup>42</sup> appear at  $504 \text{ cm}^{-1}$ , accompanied with a shoulder at  $484 \text{ cm}^{-1}$ , and  $998 \text{ cm}^{-1}$ , corresponding to the symmetric and antisymmetric stretching vibrations of BO,  $\nu_s(\text{SiOSi})$  and  $\nu_{as}(\text{SiOSi})$ , respectively. The intensity of these bands increases with increasing heat treatment time from 240 h. The band appearing at  $504 \text{ cm}^{-1}$ , characteristic of the feldspar structure, is attributed to the four-membered-ring structure in anorthite, whereas the shoulder at  $484 \text{ cm}^{-1}$ , although not well-studied, arises from the combinations of six- and three-membered-ring structures.<sup>43</sup>

### 3. DISCUSSION

The average oxygen coordination number around Si should be very close to four atoms, which is required for the formation of tetrahedral units in the network. Nevertheless, the obtained average value for  $\text{CN}_{\text{Si-O}}$  of 3.833 from the RMC simulations indicates the presence of slightly distorted tetrahedral units in the glass structure. We have also found that Al atoms are 4-fold oxygen-coordinated and have formed  $\text{AlO}_4$  tetrahedral units, as also confirmed by the  $^{27}\text{Al}$  MAS-NMR glass spectrum, similar to the basic  $\text{SiO}_4$  network units. Therefore, the formation of slightly distorted  $\text{SiO}_4$  tetrahedral units in the CMAS glass structure is likely attributable to the formation of mixed Si–O–Al chains, where Al atoms are coordinated by four oxygen atoms.

The appearance of sharp peaks at  $-71.6$  and  $-73.2$  ppm in the NMR spectra for the CMAS-GC represents two different types of dimer units, gehlenite  $\text{AlSiO}_7$ , and akermanite  $\text{Si}_2\text{O}_7$  units, respectively.<sup>37,44</sup> Because the  $^{29}\text{Si}$  MAS-NMR chemical shifts of crystalline silicates are highly sensitive to short-range order effects,<sup>35,36</sup> the presence of additional broad peaks at  $-72$  and  $-76$  ppm represents a glassy phase with structural units longer than dimers precipitated after the formation of melilite crystalline phase. This polymerization may occur because of the role of alumina, which converts NBOs to BOs through the formation of Si–O–Al linkages as postulated by Stebbins et al.<sup>45–47</sup>

In situ XRD results revealed that no additional phases were crystallized either upon heating from RT to  $900 \text{ }^\circ\text{C}$  or upon cooling from  $900 \text{ }^\circ\text{C}$  to RT. This suggests that the delayed appearance of anorthite in the CMAS-GC is mainly due to a sluggish growth mechanism.<sup>48</sup> It can be concluded, therefore, that anorthite has formed from the heterogeneous glass composition that remains after the growth of melilite-based

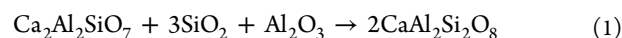
crystalline phase. However, the  $^{29}\text{Si}$  MAS-NMR spectrum of well-ordered anorthite should contain eight equally intense peaks because the structural units are composed of eight nonequivalent Si sites. As shown previously, the  $^{29}\text{Si}$  peaks can shift with higher temperature, resulting in only three overlapping peaks with a relative ratio of 3:3:2.<sup>49</sup> Therefore, the peaks in the range of  $-93$  to  $-81$  ppm (Figure 6) are assigned to the  $Q^4(4\text{Al})$  units, which are characteristics of anorthite.<sup>49</sup> On the other hand, the broad peak appearing at a more negative chemical shift can be assigned to a disordered aluminosilicate framework, which commonly contains  $0-4^{\text{IV}}\text{Al}$  units as NNNs for Si.

The peak at  $577\text{ cm}^{-1}$  in the Raman spectrum for 0 h of heat treatment is more typical of the glass structure of gehlenite, in which  $\text{Al}^{3+}$  ions act to a large extent as a network former, existing as  $(\text{AlSiO}_7)$  dimers. The broad and highly intense  $\nu_s(\text{SiO}^-)$  vibration band, in comparison to the  $\nu_s(\text{TOT})$  vibration band, in the present spectrum recorded at  $850\text{ }^\circ\text{C}$  after 0 h indicates a large distribution of  $Q^n$  units. The peak at  $926\text{ cm}^{-1}$  appears at a shift similar to that of the peak observed in the Raman spectrum of the akermanite glass.<sup>43</sup> This is expected because, as confirmed by XRD, the CMAS glass is based on the melilite solid solution. The shift in the  $\nu_s(\text{SiO}^-)$  mode toward a lower wave number, along with the decrease in the peak width with increasing heat treatment time up to 240 h, is credited to the formation of the melilite crystalline phase. It has been reported that for clinopyroxene crystalline materials containing Al, that is,  $\text{CaAl}_2\text{SiO}_6$  (CaTs), the  $\nu_s(\text{SiO}^-)$  band appears at lower frequencies ( $953\text{ cm}^{-1}$ ) than aluminum-free pyroxene,  $\text{CaMgSi}_2\text{O}_6$  ( $\sim 1000\text{ cm}^{-1}$ ).<sup>42</sup> This shift in frequency is attributed to the isomorphous substitution of  $\text{Al}^{3+}$  for  $\text{Si}^{4+}$  in the chains, resulting in longer T–O bonds ( $1.636\text{ \AA}$ ) in CaTs than the average Si–O bond length ( $1.634\text{ \AA}$ ) in diopside. In the present glass system, the small shift in frequency ( $30\text{ cm}^{-1}$ ) indicates that during the formation of crystalline phases, T–O bond lengths may increase and therefore exhibit correspondingly lower force constants.

Sharma et al.<sup>50</sup> reported that the  $\nu_s(\text{SiOSi})$  mode in Raman spectra is highly sensitive to the bond angle, bond length, and short-range connectivity.<sup>50</sup> The frequencies of the  $\nu_s(\text{TOT})$  bands in the spectra of the crystalline melilites exhibit a distinct linear relationship with the T–O–T bridging angle of the pyrosilicate unit, whereby increasing bond angle increases the resonance frequency.<sup>43</sup> In the present case, the shift in band frequency toward higher values with the increase in heat treatment time from 0 to 240 h suggests structural rearrangement around the BO through increasing the T–O–T bond angle. This increase may be due to the formation and the participation of  $\text{AlO}_4$  and  $\text{MgO}_4$  tetrahedral units in melilite crystal formation because the structure is composed of layers of  $(\text{Si},\text{Al})$  and  $(\text{Mg},\text{Al})$  tetrahedra connected by Ca in 8-fold coordination between the layers.<sup>51,52</sup> A small cation size, high field strength, and the possible existence of  $\text{MgO}_4$  tetrahedra suggest that Mg can compete with aluminum in network-forming positions. The main peak corresponding to  $\text{MgO}_4$  tetrahedral vibrations should appear at  $587\text{ cm}^{-1}$ .<sup>43,53</sup> However, because of the broadness of the spectra, features attributable to the Mg–O stretching vibrations were not identified accurately. In any case, the increase in frequency and the appearance of peaks at  $620$  and  $646\text{ cm}^{-1}$ , which are characteristic frequencies of gehlenite and akermanite crystalline phases, in the spectrum for 240 h of heat treatment confirm that  $\text{AlO}_4$  and  $\text{MgO}_4$  units participate in the formation of melilite-type gehlenite/

akermanite crystalline phase with increasing duration of heat treatment.

With a further increase in the heat treatment time from 240 to 290 h, the peak appearing at  $794\text{ cm}^{-1}$  diminishes in intensity, placing in doubt the presence of  $\text{AlO}_4$  units in the melilite solid solution.<sup>52</sup> However, the peak at  $507\text{ cm}^{-1}$ , attributable to the characteristic  $\nu_s(\text{SiOSi})$  vibration mode of anorthite crystalline phase, increases in intensity. This result suggests that a fraction of  $\text{AlO}_4$ -containing dimer units may have reacted with the glassy phase that remains after the formation of melilite crystalline phase and then converted into four-membered rings. The increase in the bandwidth of the  $\nu_s(\text{SiO}^-)$  mode further confirms the disproportion reaction  $2Q^n \rightleftharpoons Q^{n-1} + Q^{n+1}$ . Gehlenite, usually considered as an intermediate compound that becomes unstable in the presence of  $\text{SiO}_2$  and  $\text{Al}_2\text{O}_3$ , has likely reacted to give anorthite ( $\text{CaAl}_2\text{Si}_2\text{O}_8$ ) through the following reaction<sup>54,55</sup>



Moreover, on the basis of the in situ XRD results at various temperatures, it is reported that akermanite does not decompose into other compounds; otherwise, wollastonite and monticellite should appear.<sup>56,57</sup> No such crystalline phases have been encountered in the present glass system.

As already mentioned, the  $^{27}\text{Al}$  MAS-NMR spectra clearly reveal that most Al exists in the form of  $\text{AlO}_4$  units. Therefore, assuming that  $\text{Mg}^{2+}$  ions participate in the formation of melilite-like crystalline phase, the presence of four-membered rings along with eight-coordinated  $\text{Ca}^{2+}$  cations leads to the formation of crystalline anorthite from the residual glassy phase, confirmed from the presence of a band at  $327\text{ cm}^{-1}$ . The increases in the bandwidth and frequency and the decrease in the intensity of the  $\nu_s(\text{SiO}^-)$  band further confirm the structural rearrangement and disproportion reaction which occur with further increase in the heat treatment time. The decrease in the intensity can be attributed to the degree of covalence of the Al–O bonds. However, no additional crystalline phases have been observed even after 500 h of heat treatment. The presence of a broad band may, therefore, be assigned to the resonance vibrations of melilite and anorthite crystalline structural units. This clearly confirms that anorthite crystalline phase forms during the period of 240–290 h of heat treatment time from the residual phase, which is rich in  $\text{Al}_2\text{O}_3$ ,  $\text{SiO}_2$ , and  $\text{CaO}$ .

The present study clearly illustrates that the CMAS chemical composition is highly stable up to  $850\text{ }^\circ\text{C}$ , forming crystals with a composition close to that of the parent glass. Nevertheless, during prolonged heat treatment at  $850\text{ }^\circ\text{C}$ , anorthite crystallizes owing to the interaction with the glassy phase, which is rich in  $\text{Al}_2\text{O}_3$ ,  $\text{SiO}_2$ , and gehlenite crystalline units. This suggests that decreasing the concentration of  $\text{Al}_2\text{O}_3$  in the precipitated glassy phase would inhibit the formation of undesired anorthite phase. This could be realized with the partial replacement of MgO for  $\text{Al}_2\text{O}_3$  in the initial CMAS glass position. The rationale behind the selection of MgO is that it may increase the fraction of akermanite and does not much alter the properties of the CMAS glass sealing material.<sup>12</sup> Studies of such glass compositions are under progress, and the results will be reported in our forthcoming articles.

#### 4. CONCLUSIONS

The mechanism for the deleterious formation of anorthite in a melilite-based CMAS-GC composition with the potential as a

sealing material for SOFCs has been revealed from the experimental data gathered through a number of complementary advanced characterization techniques (ND, XRD, MAS-NMR, and in situ Raman). The glass network, as revealed by ND data and MAS-NMR spectra, is mainly composed of SiO<sub>4</sub> and AlO<sub>4</sub> structural units. The high stability of CMAS glass up to 850 °C was confirmed by in situ XRD. In addition to SiO<sub>4</sub> and AlO<sub>4</sub> units, quantitative XRD and MAS-NMR analyses also suggest that the melilite phase homogeneously forms along with the inclusion of MgO<sub>4</sub> tetrahedral units above the glass-transition temperature at 900 °C during the initial heat treatment period. Peaks at -72 and -76 ppm in the <sup>29</sup>Si MAS-NMR spectrum of the GC confirm that the glassy phase remaining after the melilite formation has a more polymerized structure than simple dimer units, attributable to the glass-forming role of alumina present in the remaining glass composition. The gehlenite crystalline phase in the melilite solid solution is not stable beyond 240 h of heat treatment as concluded from the decreasing intensity of the Raman peak at 794 cm<sup>-1</sup> attributed to AlO<sub>4</sub> units. A late and gradual reaction between gehlenite and the highly polymerized remaining glassy phase leads to the formation of crystalline anorthite.

## 5. EXPERIMENTAL DETAILS

**5.1. Material Preparation.** CMAS glass of composition 38.7CaO-9.7MgO-12.9Al<sub>2</sub>O<sub>3</sub>-38.7SiO<sub>2</sub> (mol %) <sup>12</sup> was prepared by melting the batch in a Pt-crucible at 1590 °C for 1 h and then quenching the glass melts in cold water. The experimental procedure for the preparation of glasses and glass powders has been detailed in our previous report. <sup>12</sup> The glass-transition temperature was observed around 730 °C. GC sample was obtained using a powder-processing technique, in which the glass powders with a mean particle size in the range 10–15 μm were pressed uniaxially (80 MPa) to form rectangular bars with dimensions of 4 mm × 5 mm × 50 mm. The as-formed rectangular glass-powder compacts were first sintered at 900 °C for 1 h and then further heat-treated at 850 °C for 500 h in air at a heating rate of 5 K min<sup>-1</sup>.

**5.2. Neutron Diffraction.** Neutron diffraction measurements were performed at the 10 MW Budapest research reactors using the two-axis position sensitive detector diffractometer (monochromatic wavelength λ<sub>0</sub> = 1.068 Å). <sup>58</sup> A powder specimen of ~3 g was placed in a cylindrical vanadium sample holder (8 mm diameter, 50 mm height, and 0.07 mm wall thickness). The diffraction pattern was measured in the momentum transfer range of 0.95 ≤ Q ≤ 9.5 Å<sup>-1</sup>. Correction and normalization procedures were utilized to obtain the structure factor, S(Q), from the raw experimental data using program packages available at the facility.

The experimental S(Q) data were simulated by the RMC method <sup>59</sup> using the software package RMC++. <sup>60</sup> The RMC method minimizes the squared difference between the experimental S(Q) and the calculated value from a three-dimensional atomic configuration. The RMC algorithm calculates the one-dimensional partial atomic pair correlation functions g<sub>ij</sub>(r), which are then inverse-Fourier-transformed to calculate the partial structure factors, S<sub>ij</sub>(Q)

$$S_{ij}(Q) = 1 + \frac{4\pi\rho_0}{Q} \int_0^{r_{\max}} r [g_{ij}(r) - 1] \sin Qr \, dr \quad (2)$$

where r<sub>max</sub> is the half edge length of the simulation box of the RMC calculation. The actual computer configuration is

modified by moving the atoms randomly until the calculated S(Q) agrees with the experimental data to within the limits of experimental error. For the RMC starting model, a disordered atomic configuration was built up with a simulation box containing 10 000 atoms. The density value was 0.070 atoms·Å<sup>-3</sup>, and the corresponding RMC half-box length was 26.13 Å. Moves are accepted only if they are in accordance with certain constraints.

Here, two types of constraints were applied to obtain a reliable three-dimensional atomic configuration, described by the partial atomic pair correlation functions, g<sub>ij</sub>(r). These included the minimum interatomic distances between atom pairs (cutoff distances) and connectivity of the network-former Si-O atom pairs, assuming that the silicon atoms are surrounded by four-coordinated oxygen atoms, forming tetrahedral SiO<sub>4</sub> units; the silicon atoms were thus required to have four oxygen neighbors at a distance of between 1.5 and 2.1 Å.

Several RMC runs were completed by modifying the cutoff distances, and the results of each run were carefully checked to obtain reliable data for each g<sub>ij</sub>(r) and coordination number distributions, CN<sub>ij</sub>(n). The partial atomic pair correlations, g<sub>ij</sub>(r), were revealed from the RMC simulation with good reproducibility and acceptable statistics.

**5.3. X-ray Diffraction.** The initiation of crystalline phase formation with temperature in the glass powders was monitored from RT to 900 °C by in situ HT-XRD, employing a Philips X'Pert diffractometer. The implemented heat treatment schedule for the hot stage was as follows: RT to 550 °C at a heating rate of 30 K min<sup>-1</sup> and from 550 to 900 °C at 5 K min<sup>-1</sup> followed by a dwell at 900 °C for 1 h. The XRD data were collected at RT, at 550 °C, and every 50 °C in the interval from 550 to 900 °C without any significant dwell. The XRD data were also collected at RT after the completion of the hot stage-heating schedule to identify the formation of any additional crystalline phases during the cooling process.

The powder XRD patterns at RT were collected using monochromatic Cu Kα<sub>1</sub> radiation over the range 15° ≤ 2θ ≤ 100° (step width of 0.02°) with a conventional Bragg-Brentano diffractometer (Philips PW3710, Ni-filter). The fraction of crystallized components in the GC after thermal treatment for 500 h was estimated by Rietveld quantitative analysis in a manner similar to that described previously. <sup>61</sup> The GCs were powdered in an agate mortar with the addition of Al<sub>2</sub>O<sub>3</sub>, which served as an internal weight standard, prior to sieving through a 60 μm mesh. Rietveld refinement was carried out with the FullProf software <sup>62</sup> using interpolation of points to model the background.

**5.4. Solid-State MAS-NMR.** <sup>27</sup>Al solid-state NMR experiments were performed on a Bruker Avance-III HD operated at a B<sub>0</sub> field of 14.1 T. The <sup>27</sup>Al (156.4 MHz) 1D experiments were carried out after a small 5° flip angle of 0.5 μs at a spinning speed of 20 kHz using a 3.2 mm MAS HFXY quadruple resonance probe (Bruker). The reference was set using a solution of AlCl<sub>3</sub> adjusted to a pH of 1 with hydrochloric acid.

<sup>29</sup>Si MAS-NMR spectra were recorded on a Bruker Avance-II spectrometer operated at 59.62 MHz (7.1 T) using a 7 mm probe at a spinning rate of 5 kHz. The one-pulse experiments were carried out with a 90° pulse length of 4.4 μs and recycle times of 60 s for CMAS glass and 1800 s for CMAS-GC. The chemical shift was referenced to TMS using N(SiMe<sub>3</sub>)<sub>3</sub> as a secondary reference.

**5.5. Raman Spectroscopy.** RT Raman spectra were obtained using a Horiba LabRAM HR 800 Evolution confocal Raman microscope, with a 532 nm excitation laser and a 100× objective lens (NA = 0.9). The incident laser power projected on the samples was ~10 mW, and the spot size was ~3.14 μm<sup>2</sup>. The collected Raman radiation was dispersed with a 600 lines-mm<sup>-1</sup> grating and focused on a Peltier-cooled charge-coupled device (CCD) detector, allowing a spectral resolution of ca. 5 cm<sup>-1</sup>. All spectra were recorded in the range 200–1200 cm<sup>-1</sup> with an integration time of 1 s and three accumulations per spectrum.

Raman spectra were collected on samples placed in a controlled-atmosphere chamber at elevated temperatures, which was recently developed for in situ studies of p-SOFC interfaces.<sup>63,64</sup> The optical system of the setup comprises a 30 mW green (532 nm) laser with 20–25 μm spot size, a polarizer which decreases the power of the laser radiation when necessary, a mechanical shutter stopping the excitation beam for system tuning, and a set of collecting lenses and mirrors. The scattered light is distributed into different directions by a 600 lines-mm<sup>-1</sup> diffraction grating monochromator MDR-12 (LOMO, Russia) and registered with a Peltier-cooled CCD camera (Princeton Instruments, 1024 × 1024 pixel resolution). The spectra were recorded in the range 70–2050 cm<sup>-1</sup> with an integration time of 1 s and 5–300 accumulations per spectrum. The measurements reported in this work were performed at 25–900 °C in atmospheric air, with glass or GC samples placed onto a single-crystal sapphire support; the accuracy of temperature control was ±1 °C.

## ■ ASSOCIATED CONTENT

### ■ Supporting Information

The Supporting Information is available free of charge on the ACS Publications website at DOI: 10.1021/acsomega.7b00598.

<sup>27</sup>Al double-quantum filtered STMAS-split-t1 spectra of CMAS glass and CMAS-GC (PDF)

## ■ AUTHOR INFORMATION

### Corresponding Authors

\*E-mail: aareddy@cgcri.res.in. Phone.: +351-234-370242. Fax: +351-234-370204 (A.R.A.).

\*E-mail: jmf@ua.pt (J.M.F.F.).

### ORCID

Amarnath R. Allu: 0000-0003-0450-0929

Sathravada Balaji: 0000-0003-0820-6444

Jürgen Senker: 0000-0002-7278-7952

José M. F. Ferreira: 0000-0002-7520-2809

### Author Contributions

A.R.A., D.U.T., and J.M.F.F. have designed the experiments. G.C.M. and M.J.P. have collected XRD data and performed the XRD refinement. F.M. has performed the ND experiments. R.S. and J.S. performed the MAS-NMR experiments. W.M. has done the in situ XRD measurements. D.A.A. and V.V.K. have performed in situ Raman measurements. A.R.A., S.B., and J.M.F.F. have compiled and analyzed all data. All authors have contributed equally in writing the manuscript.

### Notes

The authors declare no competing financial interest.

## ■ ACKNOWLEDGMENTS

This work was developed in the scope of the CICECO—Aveiro Institute of Materials (UID/CTM/50011/2013) project and partially funded by FEDER funds through the Operational Programme Competitiveness Factors (COMPETE 2020) and the Portuguese Foundation for Science and Technology (FCT). A.R.A. and S.B. gratefully acknowledges the financial support of the FCT for the fellowship grant SFRH/BD/89915/2012 and Budapest Neutron Centre, Hungary, for allotting the beam time and financial support during his visit (BRR\_407) under NMI3-II program. A.R.A. would like to thank Dr., K. Muraleedharan, Director, CSIR—CGCRI, and Dr., Ranjan Sen, Head, Glass Division, for their support and encouragement. The work of the ISSP RAS team was supported by the Ministry of Education and Science of the Russian Federation (project 14.B25.31.0018) and the Russian Foundation for Basic Research (project 13-03-12409).

## ■ REFERENCES

- Goel, A.; Reddy, A. A.; Pascual, M. J.; Gremillard, L.; Malchere, A.; Ferreira, J. M. F. Sintering Behavior of Lanthanide-Containing Glass-Ceramic Sealants for Solid Oxide Fuel Cells. *J. Mater. Chem.* **2012**, *22*, 10042.
- Reddy, A. A.; Tulyaganov, D. U.; Goel, A.; Sardo, M.; Wiper, P. V.; Pascual, M. J.; Kharton, V. V.; Kolotygin, V. A.; Tsipis, E. V.; Mafra, L.; Ferreira, J. M. F. Melilite Glass-Ceramic Sealants for Solid Oxide Fuel Cells: Effects of ZrO<sub>2</sub> Additions Assessed by Microscopy, Diffraction and Solid-State NMR. *J. Mater. Chem. A* **2013**, *1*, 6471–6480.
- Tulyaganov, D. U.; Reddy, A. A.; Kharton, V. V.; Ferreira, J. M. F. Aluminosilicate-Based Sealants for SOFCs and Other Electrochemical Applications—A Brief Review. *J. Power Sources* **2013**, *242*, 486–502.
- Reddy, A. A.; Tulyaganov, D. U.; Kharton, V. V.; Ferreira, J. M. F. Development of Bilayer Glass-Ceramic SOFC Sealants Via Optimizing the Chemical Composition of Glasses—a Review. *J. Solid State Electrochem.* **2015**, *19*, 2899–2916.
- Mahapatra, M. K.; Lu, K. Seal Glass for Solid Oxide Fuel Cells. *J. Power Sources* **2010**, *195*, 7129–7139.
- Mahapatra, M. K.; Lu, K. Glass-Based Seals for Solid Oxide Fuel and Electrolyzer Cells—A Review. *Mater. Sci. Eng., R* **2010**, *67*, 65–85.
- Lee, S. K.; Kim, H.-L.; Kim, E. J.; Mun, K. Y.; Ryu, S. Extent of Disorder in Magnesium Aluminosilicate Glasses: Insights from <sup>27</sup>Al and <sup>17</sup>O NMR. *J. Phys. Chem. C* **2016**, *120*, 737–749.
- Henderson, G. S.; Calas, G.; Stebbins, J. F. The Structure of Silicate Glasses and Melts. *Elements* **2006**, *2*, 269–273.
- Zanotto, E. D. A Bright Future for Glass-Ceramics. *Am. Ceram. Soc. Bull.* **2010**, *89*, 19–27.
- Fergus, J. W. Sealants for Solid Oxide Fuel Cells. *J. Power Sources* **2005**, *147*, 46–57.
- Meinhardt, K. D.; Kim, D.-S.; Chou, Y.-S.; Weil, K. S. Synthesis and Properties of a Barium Aluminosilicate Solid Oxide Fuel Cell Glass-Ceramic Sealant. *J. Power Sources* **2008**, *182*, 188–196.
- Reddy, A. A.; Goel, A.; Tulyaganov, D. U.; Kapoor, S.; Pradeesh, K.; Pascual, M. J.; Ferreira, J. M. F. Study of Calcium–Magnesium–Aluminum–Silicate (CMAS) Glass and Glass-Ceramic Sealant for Solid Oxide Fuel Cells. *J. Power Sources* **2013**, *231*, 203–212.
- Phillips, B. L.; Kirkpatrick, R. J. High-Temperature <sup>29</sup>Si MAS NMR Spectroscopy of Anorthite (CaAl<sub>2</sub>Si<sub>2</sub>O<sub>8</sub>) and Its P<sub>1</sub>–I<sub>1</sub> Structural Phase Transition. *Phys. Chem. Miner.* **1995**, *22*, 268–276.
- Van Tendeloo, G.; Ghose, S.; Amelinckx, S. A Dynamical Model for the P<sub>1</sub>–I<sub>1</sub> Phase Transition in Anorthite, CaAl<sub>2</sub>Si<sub>2</sub>O<sub>8</sub>. *Phys. Chem. Miner.* **1989**, *16*, 311–319.
- Daniel, I.; Gillet, P.; Ghose, S. A New High-Pressure Phase Transition in Anorthite (CaAl<sub>2</sub>Si<sub>2</sub>O<sub>8</sub>) Revealed by Raman Spectroscopy. *Am. Mineral.* **1995**, *80*, 645–648.
- Tribaudino, M.; Benna, P.; Nestola, F.; Meneghini, C.; Bruno, E. Thermodynamic Behaviour of the High-Temperature P<sub>1</sub>–I<sub>1</sub> Phase

- Transition Along the  $\text{CaAl}_2\text{Si}_2\text{O}_8$ – $\text{SrAl}_2\text{Si}_2\text{O}_8$  Join. *Phys. Chem. Miner.* **2005**, *32*, 314–321.
- (17) Czank, M.; Schulz, H. Thermal Expansion of Anorthite. *Naturwissenschaften* **1971**, *58*, 94.
- (18) Hovis, G. L.; Medford, A.; Conlon, M.; Tether, A.; Romanoski, A. Principles of Thermal Expansion in the Feldspar System. *Am. Mineral.* **2010**, *95*, 1060–1068.
- (19) Tribaudino, M.; Angel, R. J.; Cámara, F.; Nestola, F.; Pasqual, D.; Margiolaki, I. Thermal Expansion of Plagioclase Feldspars. *Contrib. Mineral. Petrol.* **2010**, *160*, 899–908.
- (20) Marques, V. M. F.; Tulyaganov, D. U.; Agathopoulos, S.; Gataullin, V. K.; Kothiyal, G. P.; Ferreira, J. M. F. Low Temperature Synthesis of Anorthite Based Glass-Ceramics Via Sintering and Crystallization of Glass-Powder Compacts. *J. Eur. Ceram. Soc.* **2006**, *26*, 2503–2510.
- (21) Guignard, M.; Cormier, L. Environments of Mg and Al in  $\text{MgO}$ – $\text{Al}_2\text{O}_3$ – $\text{SiO}_2$  Glasses: A Study Coupling Neutron and X-Ray Diffraction and Reverse Monte Carlo Modeling. *Chem. Geol.* **2008**, *256*, 111–118.
- (22) Bhatti, M. S. Y.; Gard, J. A.; Glasser, F. P. Crystallization of Anorthite from  $\text{CaO}$ – $\text{Al}_2\text{O}_3$ – $\text{SiO}_2$  Glasses. *Mineral. Mag.* **1970**, *37*, 780–789.
- (23) Reddy, A. A.; Tulyaganov, D. U.; Goel, A.; Kapoor, S.; Pascual, M. J.; Ferreira, J. M. F. Sintering and Devitrification of Glass-Powder Compacts in the Akermanite–Gehlenite System. *J. Mater. Sci.* **2013**, *48*, 4128–4136.
- (24) Orsini, P. G.; Buri, A.; Marotta, A. Devitrification of Glasses in the Akermanite–Gehlenite System. *J. Am. Ceram. Soc.* **1975**, *58*, 306.
- (25) Kempster, C. J. E.; Megaw, H. D.; Radoslovich, E. W. The Structure of Anorthite,  $\text{CaAl}_2\text{Si}_2\text{O}_8$ . I. Structure Analysis. *Acta Crystallogr.* **1962**, *15*, 1005–1017.
- (26) Reddy, A. A.; Tulyaganov, D. U.; Mather, G. C.; Rodríguez-López, S.; Das, S.; Pascual, M. J.; Muñoz, F.; Siegel, R.; Senker, J.; Ferreira, J. M. F. Influence of Strontium Oxide on Structural Transformations in Diopside-Based Glass-Ceramics Assessed by Diverse Structural Tools. *J. Phys. Chem. C* **2015**, *119*, 11482–11492.
- (27) Lee, S. K.; Stebbins, J. F. Effects of the Degree of Polymerization on the Structure of Sodium Silicate and Aluminosilicate Glasses and Melts: An  $^{17}\text{O}$  NMR Study. *Geochim. Cosmochim. Acta* **2009**, *73*, 1109–1119.
- (28) Reddy, A. A.; Goel, A.; Tulyaganov, D. U.; Sardo, M.; Mafra, L.; Pascual, M. J.; Kharton, V. V.; Tsipis, E. V.; Kolotygin, V. A.; Ferreira, J. M. F. Thermal and Mechanical Stability of Lanthanide-Containing Glass–Ceramic Sealants for Solid Oxide Fuel Cells. *J. Mater. Chem. A* **2014**, *2*, 1834–1846.
- (29) Murdoch, J. B.; Stebbins, J. F.; Carmichael, I. S. E. High-Resolution  $^{29}\text{Si}$  NMR Study of Silicate and Aluminosilicate Glasses: The Effect of Network-Modifying Cations. *Am. Mineral.* **1985**, *70*, 332–343.
- (30) Malavasi, G.; Pedone, A.; Menziani, M. C. Study of the Structural Role of Gallium and Aluminum in 45SS Bioactive Glasses by Molecular Dynamics Simulations. *J. Phys. Chem. B* **2013**, *117*, 4142–4150.
- (31) Sen, S.; Youngman, R. E. High-Resolution Multinuclear NMR Structural Study of Binary Aluminosilicate and Other Related Glasses. *J. Phys. Chem. B* **2004**, *108*, 7557–7564.
- (32) Lippmaa, E.; Maegi, M.; Samoson, A.; Tarmak, M.; Engelhardt, G. Investigation of the Structure of Zeolites by Solid-State High-Resolution silicon-29 NMR Spectroscopy. *J. Am. Chem. Soc.* **1981**, *103*, 4992–4996.
- (33) Lippmaa, E.; Maegi, M.; Samoson, A.; Engelhardt, G.; Grimmer, A. R. Structural Studies of Silicates by Solid-State High-Resolution silicon-29 NMR. *J. Am. Chem. Soc.* **1980**, *102*, 4889–4893.
- (34) Oestrike, R.; Kirkpatrick, R. J.  $^{27}\text{Al}$  and  $^{29}\text{Si}$  MASS NMR Spectroscopy of Glasses in the System Anorthite–Diopside–Forsterite. *Am. Mineral.* **1988**, *73*, 534–546.
- (35) Merwin, L. H.; Sebald, A.; Seifert, F. The Incommensurate–Commensurate Phase Transition in Akermanite,  $\text{Ca}_2\text{MgSi}_2\text{O}_7$ , Observed by in-Situ  $^{29}\text{Si}$  MAS NMR Spectroscopy. *Phys. Chem. Miner.* **1989**, *16*, 752–756.
- (36) Engelhardt, G.; Michel, D. *High-Resolution Solid-State NMR of Silicates and Zeolites*; John Wiley & Sons: Chichester, 1987; Vol. Xiv, p 485
- (37) Smith, K. A.; Kirkpatrick, R. J.; Oldfield, E.; Henderson, D. M. High-Resolution Silicon-29 Nuclear Magnetic Resonance Spectroscopic Study of Rock-Forming Silicates. *Am. Mineral.* **1983**, *68*, 1206–1215.
- (38) Kirkpatrick, R. J.; Carpenter, M. A.; Yang, W.-H.; Montez, B.  $^{29}\text{Si}$  Magic-Angle NMR Spectroscopy of Low-Temperature Ordered Plagioclase Feldspars. *Nature* **1987**, *325*, 236–238.
- (39) Phillips, B. L.; Kirkpatrick, R. J.; Carpenter, M. A. Investigation of Short-Range Al/Si Order in Synthetic Anorthite by  $^{29}\text{Si}$  MAS NMR Spectroscopy. *Am. Mineral.* **1992**, *77*, 484–494.
- (40) Oestrike, R.; Yang, W.-H.; Kirkpatrick, R. J.; Hervig, R. L.; Navrotsky, A.; Montez, B. High-Resolution  $^{23}\text{Na}$ ,  $^{27}\text{Al}$  and  $^{29}\text{Si}$  NMR Spectroscopy of Framework Aluminosilicate Glasses. *Geochim. Cosmochim. Acta* **1987**, *51*, 2199–2209.
- (41) MacKenzie, K. J. D.; Smith, M. E. Multinuclear Solid State NMR of Inorganic Materials. In *Pergamon Materials Series*; Pergamon: Elmsford, NY, 2002; pp 271–330
- (42) Sharma, S. K.; Simons, B.; Yoder, H. S., Jr. Raman Study of Anorthite, Calcium Tschermak's Pyroxene, and Gehlenite in Crystalline and Glassy States. *Am. Mineral.* **1983**, *68*, 1113–1125.
- (43) Sharma, S. K.; Yoder, H. S., Jr.; Matson, D. W. Raman Study of Some Melilites in Crystalline and Glassy States. *Geochim. Cosmochim. Acta* **1988**, *52*, 1961–1967.
- (44) Murdoch, J. B.; Stebbins, J. F.; Carmichael, I. S. E. High-Resolution  $^{29}\text{Si}$  NMR Study of Silicate and Aluminosilicate Glasses: The Effect of Network-Modifying Cations. *Am. Mineral.* **1985**, *70*, 332–343.
- (45) Stebbins, J. Aluminium Avoidance Avoided. *Nature* **1987**, *330*, 13–14.
- (46) Stebbins, J. F.; Xu, Z. NMR Evidence for Excess Non-Bridging Oxygen in an Aluminosilicate Glass. *Nature* **1997**, *390*, 60–62.
- (47) Du, W.-F.; Kuraoka, K.; Akai, T.; Yazawa, T. Study of  $\text{Al}_2\text{O}_3$  Effect on Structural Change and Phase Separation in  $\text{Na}_2\text{O}$ – $\text{B}_2\text{O}_3$ – $\text{SiO}_2$  Glass by NMR. *J. Mater. Sci.* **2000**, *35*, 4865–4871.
- (48) Tsuchiyama, A. Crystallization Kinetics in the System  $\text{CaMgSi}_2\text{O}_6$ – $\text{CaAl}_2\text{Si}_2\text{O}_8$ : The Delay in Nucleation of Diopside and Anorthite. *Am. Mineral.* **1983**, *68*, 687–698.
- (49) (a) Phillips, B. L.; Kirkpatrick, R. J. High-Temperature  $^{29}\text{Si}$  MAS NMR Spectroscopy of Anorthite ( $\text{CaAl}_2\text{Si}_2\text{O}_8$ ) and Its  $\text{P}\bar{1}$ – $\bar{1}$  Structural Phase Transition. *Phys. Chem. Miner.* **1995**, *22*, 268–276. (b) Phillips, B. L.; Kirkpatrick, R. J.; Carpenter, M. A. Investigation of Short-Range Al/Si Order in Synthetic Anorthite by  $^{29}\text{Si}$  MAS NMR Spectroscopy. *Am. Mineral.* **1992**, *77*, 484–494.
- (50) Sharma, S. K.; Mammone, J. F.; Nicol, M. F. Raman Investigation of Ring Configurations in Vitreous Silica. *Nature* **1981**, *292*, 140–141.
- (51) Neuvill, D. R.; Cormier, L.; Montouillout, V.; Florian, P.; Millot, F.; Rifflet, J.-C.; Massiot, D. Amorphous Materials: Properties, Structure, and Durability: Structure of Mg- and Mg/Ca Aluminosilicate Glasses:  $^{27}\text{Al}$  NMR and Raman Spectroscopy Investigations. *Am. Mineral.* **2008**, *93*, 1721–1731.
- (52) Merlini, M.; Gemmi, M.; Hanfland, M.; Crichton, W. High-Pressure Behavior of Akermanite and Gehlenite and Phase Stability of the Normal Structure in Melilites. *Am. Mineral.* **2009**, *94*, 704–709.
- (53) Hanuza, J.; Ptak, M.; Mączka, M.; Hermanowicz, K.; Lorenc, J.; Kaminskii, A. A. Polarized Ir and Raman Spectra of  $\text{Ca}_2\text{MgSi}_2\text{O}_7$ ,  $\text{Ca}_2\text{ZnSi}_2\text{O}_7$  and  $\text{Sr}_2\text{MgSi}_2\text{O}_7$  Single Crystals: Temperature-Dependent Studies of Commensurate to Incommensurate and Incommensurate to Normal Phase Transitions. *J. Solid State Chem.* **2012**, *191*, 90–101.
- (54) Traoré, K.; Kabré, T. S.; Blanchart, P. Gehlenite and Anorthite Crystallisation from Kaolinite and Calcite Mix. *Ceram. Int.* **2003**, *29*, 377–383.
- (55) Trindade, M. J.; Dias, M. I.; Coroado, J.; Rocha, F. Mineralogical Transformations of Calcareous Rich Clays with Firing: A Comparative

Study between Calcite and Dolomite Rich Clays from Algarve, Portugal. *Appl. Clay Sci.* **2009**, *42*, 345–355.

(56) De Wys, E. C.; Foster, W. R. The System Diopside—Anorthite—åkermanite. *Mineral. Mag.* **1958**, *31*, 736–743.

(57) de Wys, E. C. Additional Data Concerning the Stability of Åkermanite. *Mineral. Mag.* **1972**, *38*, 635–636.

(58) Sváb, E.; Mészáros, G.; Deák, F. Neutron Powder Diffractometer at the Budapest Research Reactor. *Mater. Sci. Forum* **1996**, *228–231*, 247–252.

(59) McGreevy, R. L.; Pusztai, L. Reverse Monte Carlo Simulation: A New Technique for the Determination of Disordered Structures. *Mol. Simul.* **1998**, *1*, 359–367.

(60) Fabian, M.; Svab, S.; Krezhov, K. Network Structure with Mixed Bond-Angle Linkages in  $\text{MoO}_3\text{-ZnO-B}_2\text{O}_3$  glasses: Neutron Diffraction and reverse Monte Carlo Modelling. *J. Non-Cryst. Solids* **2016**, *433*, 6–13.

(61) de Pablos-Martín, A.; Mather, G. C.; Muñoz, F.; Bhattacharyya, S.; Höche, T.; Jinschek, J. R.; Heil, T.; Durán, A.; Pascual, M. J. Design of Oxy-Fluoride Glass-Ceramics Containing  $\text{NaLaF}_4$  Nano-Crystals. *J. Non-Cryst. Solids* **2010**, *356*, 3071–3079.

(62) Rodríguez-Carvajal, J. Recent Advances in Magnetic Structure Determination by Neutron Powder Diffraction. *Phys. B* **1993**, *192*, 55–69.

(63) Agarkov, D. A.; Burmistrov, I. N.; Tsybrov, F. M.; Tartakovskii, I. I.; Kharton, V. V.; Bredikhin, S. I. Kinetics of NiO Reduction and Morphological Changes in Composite Anodes of Solid Oxide Fuel Cells: Estimate Using Raman Scattering Technique. *Russ. J. Electrochem.* **2016**, *52*, 600–605.

(64) Agarkov, D.; Burmistrov, I.; Tsybrov, F.; Tartakovskii, I.; Kharton, V.; Bredikhin, S.; Kveder, V. Analysis of Interfacial Processes at the SOFC Electrodes by *in-Situ* Raman Spectroscopy. *ECS Trans.* **2015**, *68*, 2093–2103.